ACS APPLIED MATERIALS & INTERFACES

www.acsami.org

Research Article

Controllable CVD Growth of 2D Cr_5Te_8 Nanosheets with Thickness-Dependent Magnetic Domains

Hanxiang Wu, Jianfeng Guo, Suonan Zhaxi, Hua Xu, Shuo Mi, Le Wang, Shanshan Chen, Rui Xu, Wei Ji, Fei Pang,* and Zhihai Cheng*

Cite This: *ACS Appl. Mater. Interfaces* 2023, 15, 26148−26158

Read Online

ACCESS | Metrics & More | Article Recommendations | Supporting Information

ABSTRACT: As a unique 2D magnetic material with self-intercalated structure, Cr_5Te_8 exhibits many intriguing magnetic properties. While its ferromagnetism of Cr_5Te_8 has been previously reported, the research on its magnetic domain remains unexplored. Herein, we have successfully fabricated 2D Cr_5Te_8 nanosheets with controlled thickness and lateral size by chemical vapor deposition (CVD). Then magnetic property measurement system revealed Cr_5Te_8 nanosheets exhibiting intense out-of-plane ferromagnetism with a Curie temperature (T_C) of 176 K. Significantly, we reported for the first time two magnetic domains: magnetic bubbles and thickness-dependent maze-like magnetic domains in our Cr_5Te_8 nanosheets by cryogenic magnetic force microscopy (MFM). The domain width of the maze-like magnetic domains increases rapidly with decreasing sample thickness; meanwhile, the domain contrast decreases. This indicates the dominant role of ferromagnetism shifts from dipolar interactions to magnetic anisotropy. Our research not only establishes a pathway for the controllable growth of 2D magnetic materials but also points toward novel avenues for regulating magnetic phases and methodically tuning domain characteristics.

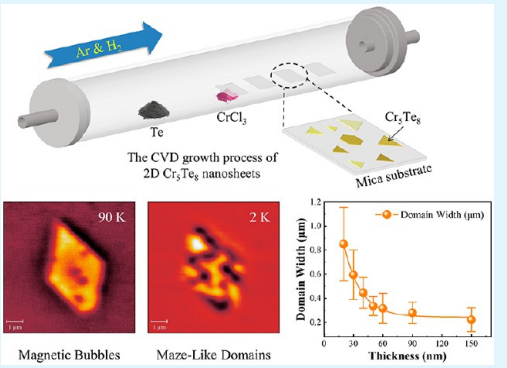

KEYWORDS: *Cr_5Te_8, 2D magnetic materials, chemical vapor deposition, maze-like magnetic domain, magnetic bubbles*

1. INTRODUCTION

As a crucial component of the 2D material family, due to the promising application prospect in spintronics and magnetic memory devices,[1,2] 2D magnetic materials with exceptional electrical[3,4] and photoelectrical[5,6] properties as well as novel magnetic[7−9] properties have received extensive attention. Particularly, it is found that monolayer Fe_3GeTe_2 still retained ferromagnetic long-range order at low temperatures.[10−12] Thus far, ultrathin $Cr_xGa_{1-x}Te$ nanosheets have exhibited intrinsic room-temperature ferromagnetism, which renders them ideal candidates for carrier control.[13] Despite 2D magnetic materials hold promising prospects for exploration and practical applications, its magnetic behavior especially in the magnetic domain structure is still in its nascent stages. Consequently, it is essential to explore the controllable growth and the magnetic domain structure of 2D magnetic materials.

Remarkably, Cr-based chalcogenides exhibit a vast array of self-intercalated phases and thickness-dependent properties due to their diverse compositions, structures as well as novel magnetic properties for fundamental study and promising technological applications.[14−31] Particularly, the 2D Cr_5Te_8 nanosheet was demonstrated to be ferromagnetic with strong out-of-plane spin polarization, and Curie temperature (T_C) increases monotonously from 100 K in the thin flake (10 nm) to 160 K in the thick flake (30 nm), which arises from the pivotal role of the strong interlayer coupling of the magnetic order.[32−39] Nevertheless, the controllable growth of high-quality 2D Cr_5Te_8 remains an immense challenge. The chemical vapor deposition (CVD) method has unique advantages in the preparation and phase-selective growth of nonlayered materials. Indeed, multifarious kinds of nonlayered nanoflakes such as Cr_2S_3,[40−44] MnSe,[45,46] Fe_7Se_8[47] and CoSe[48] have been obtained by CVD. Hence, CVD presents a feasible avenue for fabricating high-quality, nonlayered 2D Cr_5Te_8 nanosheets.

To date, several groups have synthesized 2D Cr_5Te_8 crystals using CVD[32−36] and found the Cr_5Te_8 to be an air-stable ultrathin crystal with a thickness-tunable T_C;[32] phase-selective growth of trigonal Cr_5Te_8 (tr-Cr_5Te_8) and monoclinic Cr_5Te_8 (m-Cr_5Te_8) crystals was obtained.[35] Various van der Waals (vdW) vertical heterostructures with Moiré superlattice were fabricated.[33,34] Furthermore, the geometrically frustrated structure in Cr_5Te_8 crystal is related to the large anomalous

Received: February 24, 2023
Accepted: May 7, 2023
Published: May 19, 2023

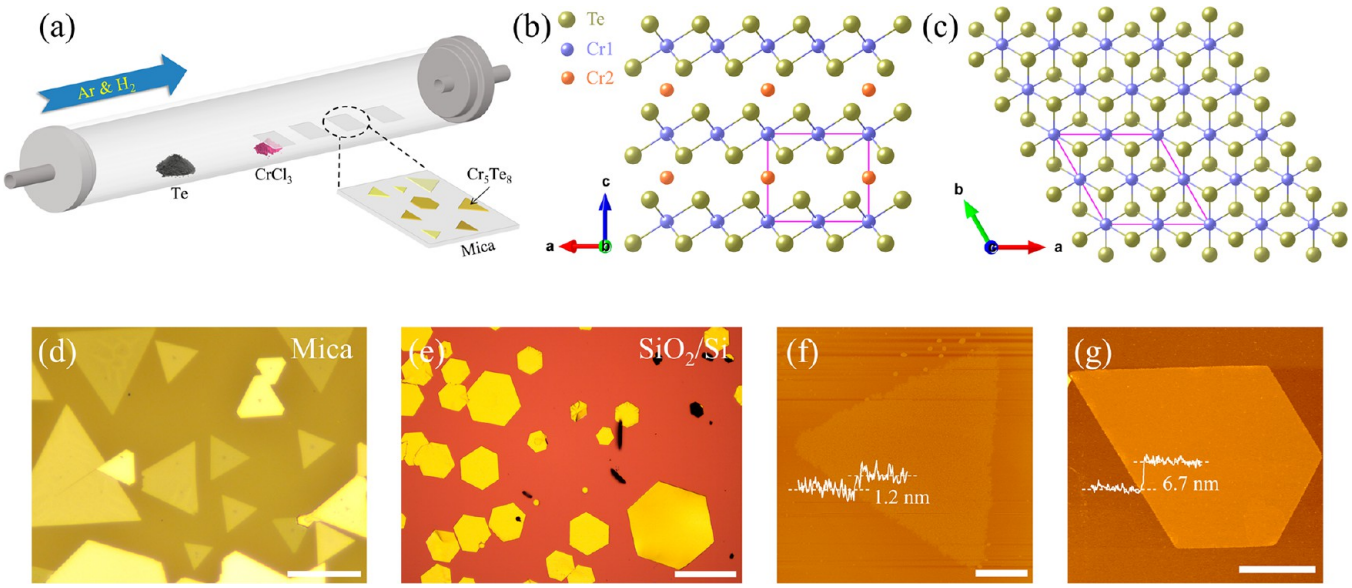

Figure 1. Growth method and morphology characterization of Cr_5Te_8 nanosheets. (a) Schematic diagram of the CVD setup for synthesis of Cr_5Te_8 nanosheets. (b, c) Crystal structure (side (b) and top (c) views) of Cr_5Te_8 obtained by CVD. (d, e) Typical OM images of Cr_5Te_8 grown on mica (d) and SiO_2/Si (e) substrates. The scale bars are 30 and 200 μm, respectively. (f, g) AFM images and corresponding height profiles of Cr_5Te_8 nanosheets grown on mica (f) and SiO_2/Si (g) substrates. The scale bars are 5 μm.

Hall effect (AHE), which is a favorable factor for the construction of novel nondissipative spintronic devices.[35] The manipulation of magnetic moments under different magnitudes of magnetic excitation is demonstrated in the Cr_2Te_3−Cr_5Te_8 lateral heterojunction.[36] Herein, we reported the controllable growth of 2D self-intercalated Cr_5Te_8 nanosheets via CVD and found temperature and source−substrate distance (D_{SS}) are key parameters for synthesis of 2D Cr_5Te_8 nanosheets. Furthermore, we found two distinct magnetic domain structures: magnetic bubbles and thickness-dependent maze-like magnetic domains by magnetic force microscopy (MFM). Optical microscopy (OM), atomic force microscopy (AFM), X-ray diffraction (XRD), scanning electron microscopy (SEM) with energy dispersive spectroscopy (EDS), Raman, and X-ray photoelectron spectroscopy (XPS) measurements illustrated the high crystallinity and accurate composition of the grown 2D Cr_5Te_8 nanosheets. Additionally, magnetic property measurement system (MPMS) measurements demonstrated that Cr_5Te_8 nanosheets exhibit both out-of-plane and in-plane ferromagnetism with a T_C ranging from 160 to 176 K, which was lower than those previously reported in bulk samples.[49] Moreover, we also studied the thickness-dependent maze-like magnetic domains by MFM. The first discovery of the strong thickness-dependent behavior of the domain width and domain contrast of the maze-like magnetic domain in 2D Cr_5Te_8 presents a promising avenue for their practical application in magnetic memory devices and other ferromagnetism-pertinent fields. Meanwhile, this work would also provide a valuable reference for the controllable growth and the exploration of the magnetic domain structure of other nonlayered 2D magnetic materials, thereby paving the way for further research on these 2D magnetic materials and their magnetism-pertinent applications in spintronics and magnetic memory devices.

2. RESULTS AND DISCUSSION

The schematic diagram of the CVD growth process of Cr_5Te_8 nanosheets is described in Figure 1a (Figure S1, Supporting Information), which enables to precisely control the nucleation density and lateral size of Cr_5Te_8 nanosheets on mica and SiO_2/Si substrates. The crystal structure of Cr_5Te_8 is shown in Figure 1b,c, displaying a self-intercalated crystal structure intercalating Cr atoms into the vdW gap between the $CrTe_2$ layers.[38,39] Typical OM images of Cr_5Te_8 are shown in Figure 1d,e. The Cr_5Te_8 nanosheets appear as predominantly triangular on mica and hexagonal on SiO_2/Si. Notably, the Cr_5Te_8 nanosheets on mica are universally thinner than those on SiO_2/Si, potentially due to the presence of numerous suspended bonds on SiO_2/Si substrates. In addition to mica and SiO_2/Si substrates, we also synthesized 2D Cr_5Te_8 nanosheets on sapphire substrates (Figure S2). The thickness of Cr_5Te_8 nanosheets is shown in Figure 1f,g. Compared with the *c*-axis length of 0.60 nm,[32] the grown sample in Figure 1f is a bilayer nanosheet with a lateral size of approximately 25 μm. OM and SEM images corresponding to Figure 1f,g are presented in Figure S3. OM image and AFM morphology of a typical hexagonal Cr_5Te_8 nanosheet with a thickness of 9.4 nm grown on the mica substrate are shown in Figure S4.

To examine the crystal phase of the as-synthesized Cr_5Te_8 nanosheets, their composition and structure were characterized. A large-scale SEM image of Cr_5Te_8 nanosheets with a maximum lateral size reaching 300 μm is shown in Figure 2a. To examine the crystal phase of the as-synthesized Cr_5Te_8 nanosheets, XRD characterization was performed. The XRD pattern of 2D Cr_5Te_8 is shown in Figure 2b. Four diffraction peaks located at 14.8°, 29.7°, 45.2°, and 61.5° are indexed to the (002), (004), (006), and (008) diffraction planes which matches well with the trigonal Cr_5Te_8 standard PDF card (PDF#50-1153). This highlights the accuracy of the structure of as-grown 2D Cr_5Te_8.[38,39] Furthermore, only (00*X*) peaks appear in the XRD pattern, which suggested the surface of the Cr_5Te_8 crystal is parallel to the *ab*-plane. Further EDS was

https://doi.org/10.1021/acsami.3c02446
ACS Appl. Mater. Interfaces 2023, 15, 26148−26158

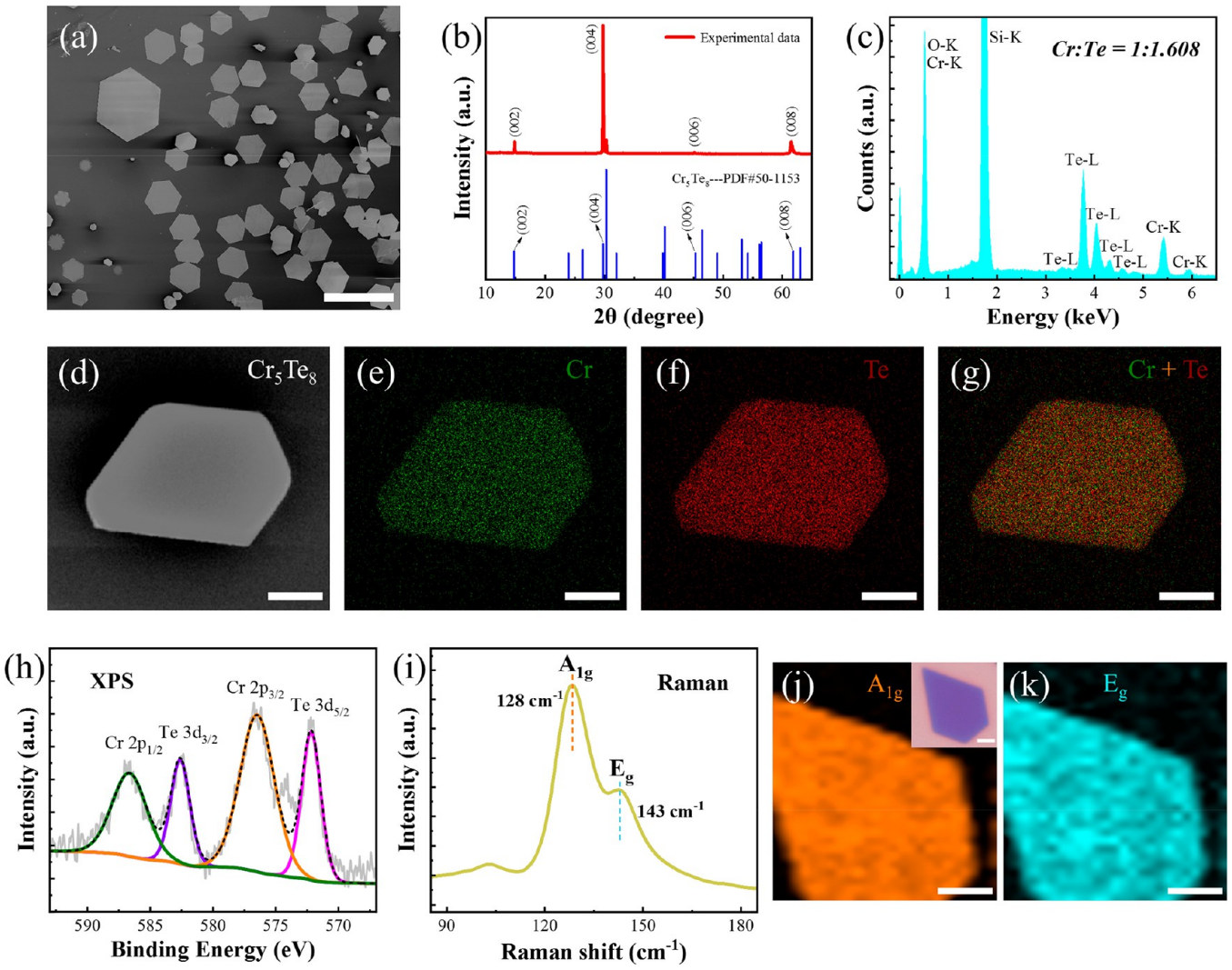

Figure 2. Composition and structure characterization of CVD-grown Cr_5Te_8 nanosheets. (a) Large-scale SEM image of Cr_5Te_8 nanosheets. The scale bar is 300 μm. (b) XRD patterns of as-grown Cr_5Te_8 nanosheets (top) and the standard Cr_5Te_8 crystal from PDF card (bottom). (c) EDS analysis of CVD-grown Cr_5Te_8 nanosheets. (d–g) SEM image (d) of a hexagonal Cr_5Te_8 nanosheet and corresponding EDS mapping of Cr element (e), Te element (f), and an overlay of Cr and Te elements (g). (h) XPS of as-grown Cr_5Te_8 nanosheets. (i) Raman spectrum of a Cr_5Te_8 nanosheet with a thickness of 6.7 nm. (j, k) Raman mapping correlated to Raman peaks at 128 cm^{-1} (j) and 143 cm^{-1} (k) corresponding to A_{1g} and E_g modes. The inset shows the corresponding OM image of the Cr_5Te_8 nanosheet. The scale bars of (d–g) and (j, k) are 2 μm.

employed to analyze the elemental composition of the CVD-grown Cr_5Te_8 nanosheets. As shown in Figure 2c, the atomic ratio of Cr to Te is approximately 1:1.608, which is extremely close to 5:8, consistent with the stoichiometric ratio of Cr_5Te_8. EDS mapping of Cr and Te elements is shown in Figure 2d–g, whose uniform color distribution manifests the formation of Cr_5Te_8 crystal, indicating the uniformity of spatial distribution of its components. XPS was utilized to examine the chemical composition and bonding type of the CVD-grown Cr_5Te_8. As shown in Figure 2h, the peaks located at binding energies of ≈576.47 and 586.64 eV are attributed to Cr $2p_{3/2}$ and Cr $2p_{1/2}$, and the peaks located at ≈572.17 and 582.6 eV are attributed to Te $3d_{5/2}$ and Te $3d_{3/2}$, indicating a $Cr^{3.2+}$ state and a Te^{2-} state,[32] well consistent with the Cr_5Te_8 crystal, respectively. Eventually, Raman spectrum was performed in a Cr_5Te_8 nanosheet with a thickness of 6.7 nm, as presented in Figure 2i. Two prominent peak positions at 128 and 143 cm^{-1} corresponding to A_{1g} and E_g modes appear for the Cr_5Te_8 nanosheet, respectively. Raman mapping correlated to Raman peaks at 128 and 143 cm^{-1} corresponding to A_{1g} and E_g modes is shown in Figure 2j,k, whose homogeneous contrast with background further demonstrates the high uniformity of as-grown Cr_5Te_8 nanosheets. Overall, all these results confirm that 2D Cr_5Te_8 nanosheets with high quality and accurate composition were successfully synthesized, providing a brilliant material foundation for further research on the controllable growth and magnetic behavior.

In order to achieve controllable growth of Cr_5Te_8 nanosheets, systematic experiments were carried out. It was found that growth temperature and D_{SS} between the $CrCl_3$ source and mica substrate are crucial for controlling average lateral size, nucleation density, and coverage of Cr_5Te_8 nanosheets. To investigate the effect of growth temperature, the other growth parameters (carrier gas and D_{SS} = 4 cm) were kept constant, and the temperature of Te powder was held steady at 550 °C. Cr_5Te_8 nanosheets on mica grown at different temperatures exhibit significant variation in average lateral sizes and nucleation densities. Typical OM images of Cr_5Te_8 grown

https://doi.org/10.1021/acsami.3c02446
ACS Appl. Mater. Interfaces 2023, 15, 26148–26158

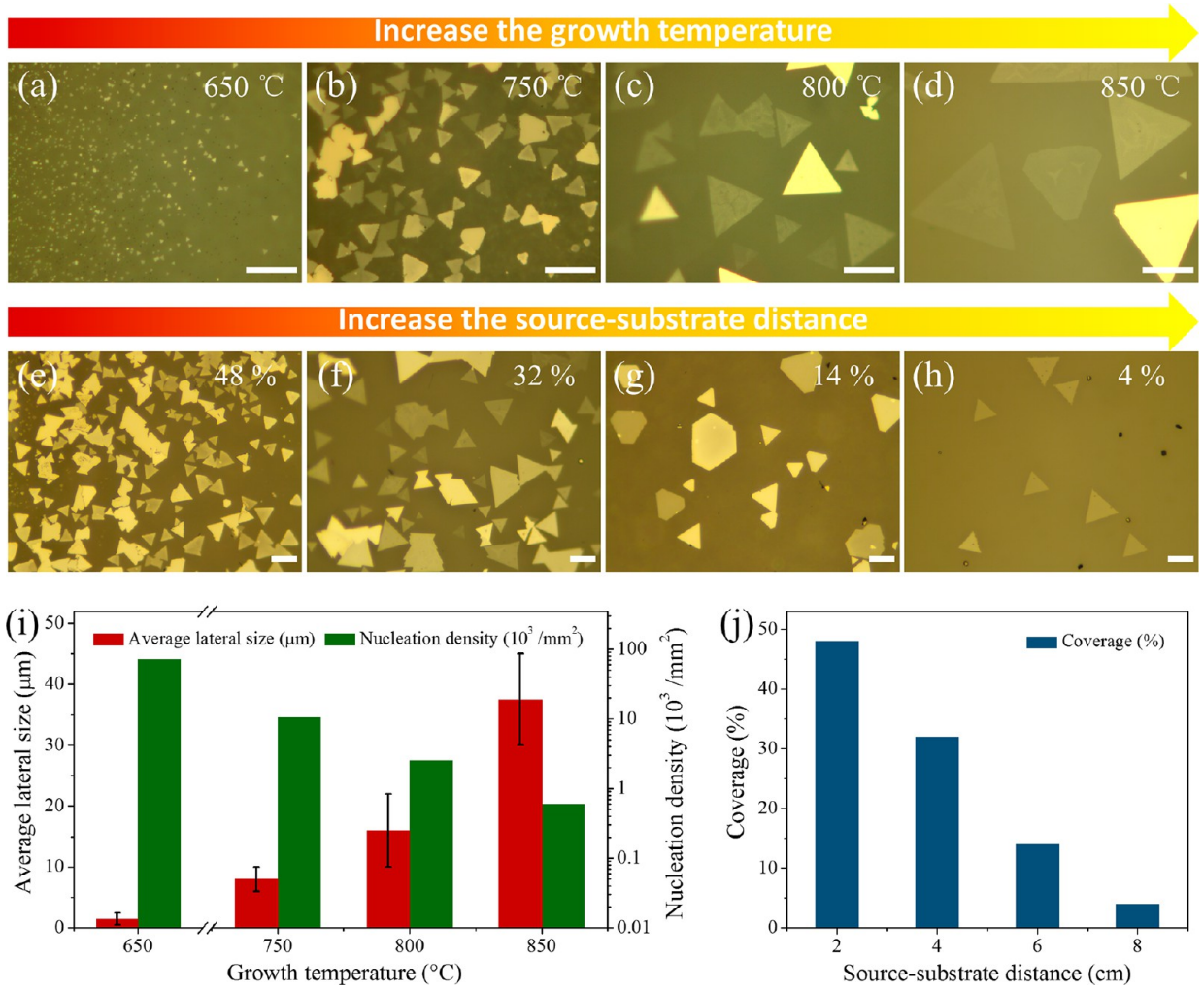

Figure 3. Controllable growth of Cr_5Te_8 nanosheets on mica. (a–d) OM images of Cr_5Te_8 nanosheets at different growth temperatures: 650 (a), 750 (b), 800 (c), and 850 °C (d). (e–h) OM images of Cr_5Te_8 nanosheets synthesized under the same growth temperature at 800 °C with coverage of ≈48%, 32%, 14%, and 4% for different D_{SS} of ≈2 (e), 4 (f), 6 (g), and 8 cm (h), respectively. Scale bars: 20 μm. (i) Histogram of average lateral size (red bar) and nucleation density (green bar) with variational growth temperature corresponding to (a–d). (j) Histogram of coverage (blue bar) with variational D_{SS} corresponding to (e–h).

on mica at different growth temperatures are presented in Figure 3a–d. When the growth temperature is 650 °C, the especially small average lateral size about 1.5 μm and high nucleation density of about 72500/mm^2 remain. Because the temperature (650 °C) is lower than the evaporation temperature of the $CrCl_3$ source, there is no sufficient amount of the reactants. Increasing growth temperature to 750 °C, the average lateral size remains rapidly increasing up to about 8 μm, while the nucleation density dramatically reduces to 10500/mm^2, which implies an adequate supply of reaction sources at the appropriate growth temperature. At a higher growth temperature (800 °C), the average lateral size continues to increase, reaching about 16 μm, and the nucleation density is continuously reduced at 2500/mm^2. When the growth temperature is kept considerably high at 850 °C, the average lateral size gets extremely big, approximately 37.5 μm, while the comparatively exceptionally low nucleation density of about 600/mm^2 is obtained, which provides a valuable insight into the growth of large single crystals. As shown in Figure 3i, growth temperature has a significant effect on the Cr_5Te_8 size and nucleation density. These findings are in accord with the nucleation model of vapor deposition presented by Burton et al., which proposes that the growth temperature is positively correlated to the transverse size, but negatively with nucleation probability.[50] Specifically, at lower growth temperature, the growth is primarily controlled by kinetics, resulting in higher nucleation density and smaller nanosheets, whereas at higher growth temperature, the growth is mainly controlled by thermodynamics, leading to reduced nucleation density to generate larger nanosheets.

Furthermore, we also identified D_{SS} as an essential parameter in controlling the coverage of Cr_5Te_8 nanosheets. With constant growth parameters (carrier gas and growth temperature) maintained, and growth temperature set at 800 °C, the Cr_5Te_8 nanosheets on mica synthesized at different D_{SS} exhibit distinct changes in their coverages shown in Figure 3e–h. As shown in the histogram of Figure 3j, with increasing D_{SS} from 2 to 8 cm, the coverage of Cr_5Te_8 on the mica substrates decreased from 48% to 4%. It is attributed to the low effective source concentration with increasing distance, causing differential coverage between upstream and downstream locations. The remarkable effect of D_{SS} on the growth process of Cr_5Te_8 has also been observed in other 2D materials.[18]

https://doi.org/10.1021/acsami.3c02446
ACS Appl. Mater. Interfaces 2023, 15, 26148–26158

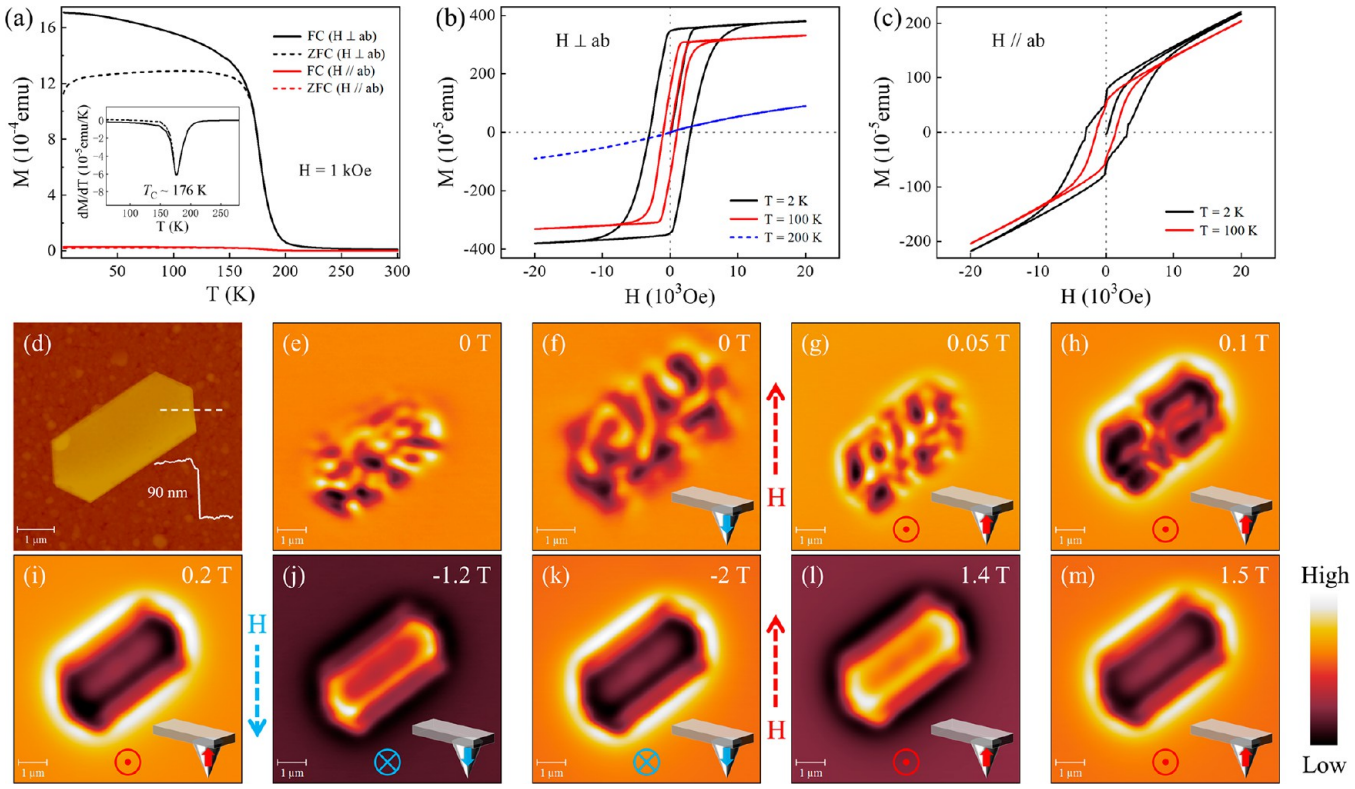

Figure 4. Ferromagnetism of Cr_5Te_8 nanosheets. (a) Temperature-dependent magnetic moments $M-T$ with the magnetic field perpendicular (black line) and parallel (red line) to the *ab*-plane for both the FC (solid line) process and the ZFC (dashed line) process on the sample under an external field of 1000 Oe. The insets show the first-order derivatives of M with respect to T to derive the T_C of Cr_5Te_8 ($H\perp ab$). (b, c) Magnetic-field-dependent magnetic moments $M-H$ at 2, 100, and 200 K with the magnetic field perpendicular. (d) AFM topography of a Cr_5Te_8 single nanosheet. (e−m) Maze-like magnetic domains (e, f) and evolution (g−m) of the Cr_5Te_8 single nanosheet at 2 K after a ZFC procedure with the external magnetic field ranged from −2 to 1.5 T. The coercivity of the MFM tip is approximately 400 Oe. A circle with a dot represents the magnetic field pointing outward (perpendicular to the plane of the sample), while a circle with a cross represents the magnetic field pointing inward (perpendicular to the plane of the sample). The red and blue dotted arrows represent the direction of the applied magnetic field, with red indicating a vertically upward direction and blue indicating a vertically downward direction. The color scales are 23 (e, f), 32 (g, j), 52 (h, i), 74 (k, m), and 92 deg (l).

In order to probe the magnetic properties of as-synthesized Cr_5Te_8 nanosheets, the magnetic susceptibility of 2D Cr_5Te_8 on mica was measured by MPMS. To prevent possible magnetic contamination, the samples were handled with only plastic tweezers. As shown in Figure 4a, the temperature-dependent magnetization moments ($M-T$) with the magnetic field perpendicular ($H\perp ab$) and parallel ($H\|ab$) to the *ab*-plane for both the field-cooling (FC) process and the zero-field-cooling (ZFC) process were performed on the samples under an external field of 1 kOe. The $M-T$ data demonstrates a transition from paramagnetic to ferromagnetic below T_C, which indicates the apparent ferromagnetic nature of synthesized 2D Cr_5Te_8 samples. The first-order derivative of $M-T$ ($H\perp ab$) in the inset confirms that Cr_5Te_8 nanosheets possess a magnetic phase transition at $T_C \sim 176$ K, which is lower than previous reports on bulk samples.[49] Additionally, the magnetization under a perpendicular field ($H\perp ab$) is notably greater than that under a parallel field ($H\|ab$). This suggests that the *c*-axis serves as the magnetic easy axis, indicating a ferromagnetic order with enhanced perpendicular magnetic anisotropy.

There are several potential mechanisms that could account for the reduced T_C observed in the Cr_5Te_8 nanosheets. First, the increased proportion of surface atoms may lead to a slight change in the stoichiometry of Cr and Te elements, which can be regarded as a doping effect. The doping effect can tune ferromagnetism in the 2D limit. When the nanosheets become thinner, Te element content on the surface will be changed, resulting in a more significant T_C deviation from the bulk.[51,52] This is accordance with Haraldsen's pioneering theory, in which the T_C of chromium telluride system shows an excessively gigantic sensitivity to Te element content.[51] Second, surface atoms may undergo reconstruction that changes the interatomic distance and thus the ferromagnetic interaction, as previously reported in 2D Cr_2Te_3.[28] Third, the ferromagnetic interaction may change due to the stress imposed on Cr_5Te_8 nanosheets originating from the mismatch lattice constant between the mica substrate and Cr_5Te_8 nanosheets, leading to a change in T_C.[27]

The magnetic field dependent magnetic moments ($M-H$) further confirmed the ferromagnetism and magnetic anisotropy. $M-H$ values at different temperatures with $H\perp ab$ and $H\|ab$ are presented in Figures 4b and 4c, respectively. Large magnetic hysteresis loops when $H\perp ab$ and much smaller loops when $H\|ab$, further confirmed that the *c*-axis is the magnetic easy axis. Notably, the $M-H$ curve exhibits step-like features in Figure 4c. We infer that the step of $M-H$ curves may associate with a complex magnetic domain structure and near degeneracy of magnetic orderings with a continuously varying canting from the *c*-axis ferromagnetic, which is usually

https://doi.org/10.1021/acsami.3c02446
ACS Appl. Mater. Interfaces 2023, 15, 26148−26158

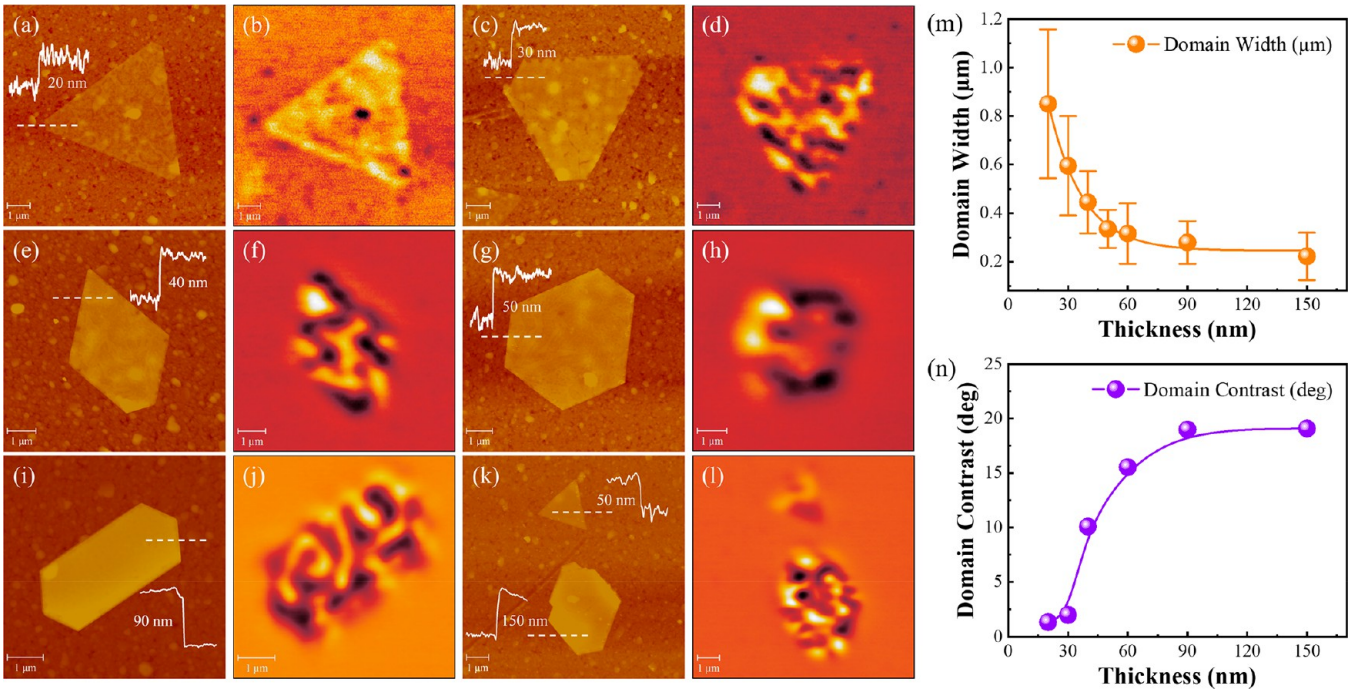

Figure 5. Maze-like magnetic domains of Cr_5Te_8 nanosheets with different thickness. (a–l) AFM topographies (a, c, e, g, i, k) and corresponding MFM images (b, d, f, h, j, l) of Cr_5Te_8 nanosheets with different thickness at 2 K. The color scales are 2.6 (b, d), 10 (f), 7.2 (h), 23 (j), and 19 deg (l). (m, n) Domain width (m) and domain contrast (n) of the maze-like magnetic domains as variables of the thickness of Cr_5Te_8 nanosheets.

observed in the relatively thick 2D magnetic materials.[19,23] Furthermore, $M-T$ and $M-H$ for the thinner nanosheets grown on a mica substrate are depicted in Figure S5, revealing a T_C of 160 K. It is consistent with the magnetic phase diagram of the layer number versus the temperature of Cr_5Te_8 single crystals.[32]

Because the thickness of Cr_5Te_8 nanosheets are not fully uniform, MPMS results are an averaged magnetic signal of different thickness nanosheets. In order to determine the ferromagnetic signal in a single Cr_5Te_8 nanosheet with well-defined thickness, the magnetic domain structures of Cr_5Te_8 nanosheets were characterized by cryogenic MFM. With nanoscale magnetic signal resolution facilitating the detection of even very small magnetic signals, the MFM can provide real-space magnetic domain signals from individual Cr_5Te_8 nanosheets.[53]

The AFM topography of a 90 nm thick hexagonal Cr_5Te_8 nanosheet characterized by MFM is shown in Figure 4d. Figure 4e–m (Figure S6) shows the evolution process of its magnetic domain structure under different magnetic fields. To observe the magnetic structures, the nanosheet was first cooled by ZFC from room temperature to 2 K. Obviously, the magnetic domain structure is different after every ZFC process, as shown in Figure 4e (after the first ZFC procedure) and Figure 4f (after another ZFC procedure). This random formation process of magnetic domains confirms that the signals measured by MFM are indeed magnetic signals. In addition, the domain structure formed by spontaneous magnetization of the nanosheet after the ZFC process is a maze-like domain as shown in Figure 4e,f. Each domain of the Cr_5Te_8 nanosheet is about 3 μm in length, 280 nm in width, and 19° in domain contrast.

Subsequently, an external magnetic field perpendicular to the *ab*-plane ($H\perp ab$) was applied to the Cr_5Te_8 nanosheet at 2 K, and the dynamic evolution of the maze-like magnetic domains was characterized. When the magnetic field increased gradually from 0 to 0.2 T, significant changes were observed in the magnetic domain structure as shown in Figure 4f–i. Specifically, as the magnetic field intensified, the size of the magnetic domains parallel to the direction of the field progressively expands. When the additional magnetic field is increased to 0.1 T, the dark-contrast domains cover a significant portion of the nanosheet, leaving only a few bright-contrast maze-like domains in the central region. When the additional magnetic field increases to 0.2 T, the dark-contrast domain region further expands and saturates, forming a full dark single domain that fills the entire nanosheet. Notably, the contrast within this single domain is nonuniform, with darker contrast in the central regions and brighter contrast in the edge regions, probably due to the anisotropy of the nanosheet shape and the broken translational symmetry in the edge regions. When domain region saturates, a re-entrant stray field outside of the nanosheet was created.[54] The MFM signal reached a maximum at nanosheet borders (edge regions) where the magnetization or the thickness is discontinuous. In contrast, it is minimum in the central regions of the nanosheets, which is similar to a uniformly magnetized infinite plane without generating any stray field.[54,55]

As shown in Figure 4j,k, the magnetic field direction was reversed. When the field was increased to −2 T, the MFM image also reversed in Figure 4k from full brightness to full darkness, which indicated a reversal of the magnetization direction of the nanosheet. The direction of the additional magnetic field then reverses again. From 1.4 to 1.5 T in Figure 4l,m, the magnetic signal as a whole is reversed, and the reversal of the magnetic domains does not evolve dynamically. The above evolution process of the magnetic domain of the Cr_5Te_8 single nanosheet with the applied magnetic field is completely consistent with the changing trend of the $M-H$ curve of the mass magnetic signal of multi-nanosheets,

https://doi.org/10.1021/acsami.3c02446
ACS Appl. Mater. Interfaces 2023, 15, 26148−26158

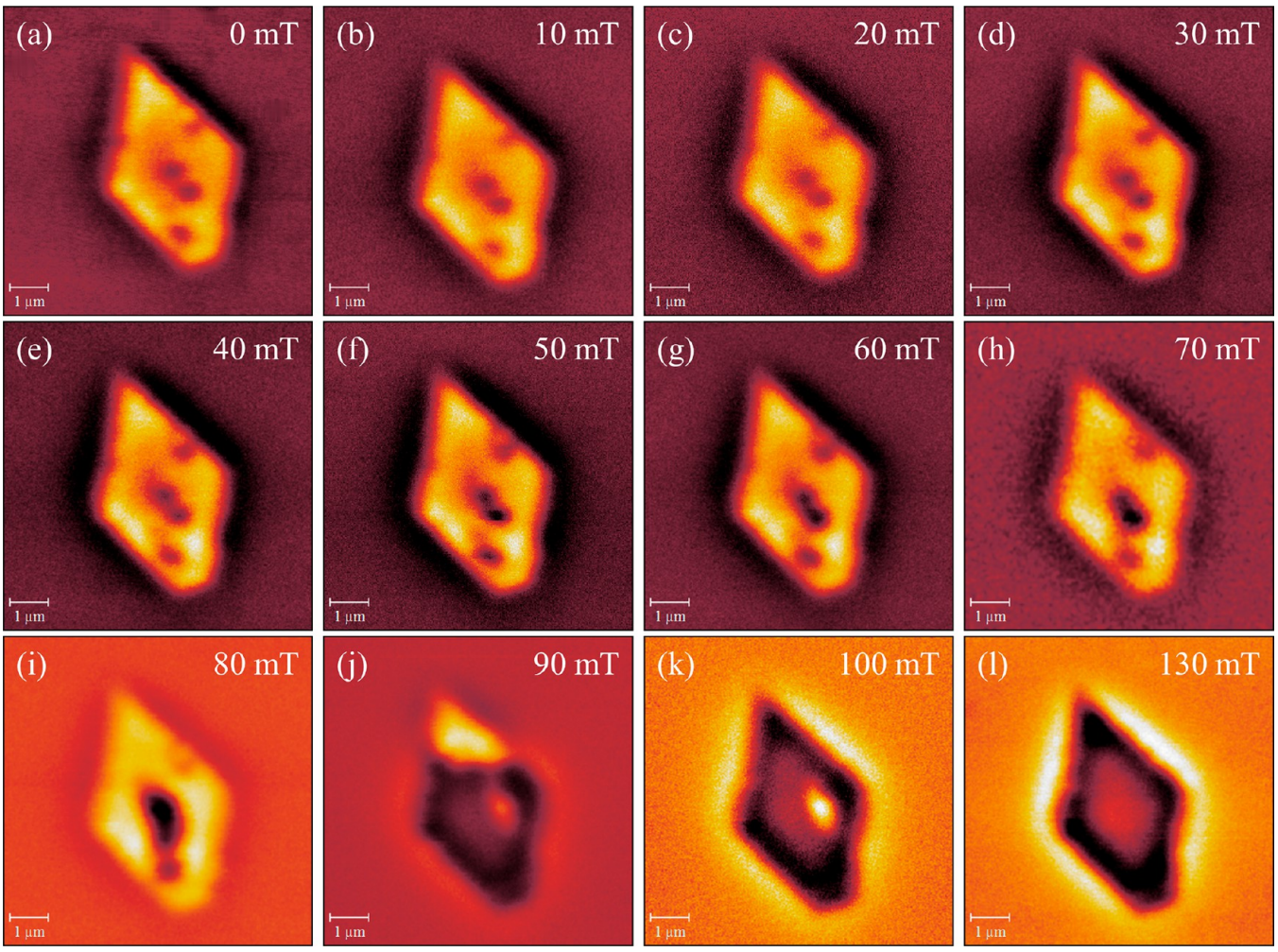

Figure 6. Evolution of magnetic bubbles in 2D Cr_5Te_8. (a) Magnetic bubbles of a Cr_5Te_8 single nanosheet at 90 K after ZFC. (b–l) Existence stabilized (b–f), merging (g–i), expansion (j), inversion (k), and saturation (l) of magnetic bubbles with the external magnetic field ranging from 0 to 130 mT. The color scales are 1.4 (a, h, k, l), 1.1 (b, c), 1.2 (d, e, f), 1.3 (g), 3 (i), and 2.8 deg (j).

indicating that the as-grown Cr_5Te_8 nanosheet has a distinguished hard magnetism. In addition, Figure 4l,m also shows that the coercivity field of the Cr_5Te_8 nanosheet is between 1.4 and 1.5 T.

Then the magnetic domain structures of Cr_5Te_8 nanosheets with different thickness were systematically characterized by MFM. Figure 5a–l (Figure S7) shows the AFM morphologies and corresponding MFM images at 2 K after ZFC. It can be found that maze-like magnetic domains varied with the thickness. To quantitatively analyze the magnetic signal, we compared the domain width and domain contrast of these maze-like domains and found a strong thickness dependence. With increasing nanosheet thickness from 20 to 150 nm, magnetic domain width decreases from 850 to 220 nm, which presents a very wide adjustable range as shown in Figure 5m.

The maze-like magnetic domains indicated the dominant role of dipole interaction was greater than magnetic anisotropy and exchange interaction in the Cr_5Te_8 nanosheets.[56] Assuming ferromagnetic coupling between the Cr_5Te_8 layers along the *c*-axis, the nanosheets can be described by the following Hamiltonian:[57,58]

$$H = \frac{J}{2}\int [\nabla\cdot\vec{n}(\vec{x})]^2\, \mathrm{d}^2\vec{x} - K\int {n_z}^2(\vec{x})\, \mathrm{d}^2\vec{x} - \frac{\Omega}{4}\frac{[\vec{n}(\vec{x}) - \vec{n}(\vec{x}')]^2 - 3\{\vec{v}\cdot[\vec{n}(\vec{x}) - \vec{n}(\vec{x}')]\}}{|\vec{x} - \vec{x}'|^3}\, \mathrm{d}^2\vec{x}\, \mathrm{d}^2\vec{x}' \quad (1)$$

where J is the Heisenberg exchange interaction, $\vec{n}(\vec{x})$ is the unit vector of the magnetization at position $\vec{x}$ on a 2D plane, K is the overall magnetic anisotropy, Ω is the dipolar interaction strength, and $\vec{v}$ is the unit vector from $\vec{x}$ to $\vec{x}'$. In the 2D limit, when the dipole interaction dominates the magnetic anisotropy, the dipole interaction should stabilize a maze-like domain structure with a domain width of $\sim J/\Omega$ (on the order of 100 nm for most ferromagnetic materials).[57,59] With decreasing the thickness of Cr_5Te_8 nanosheets, the magnetic anisotropy gradually increases to dominate the dipolar interaction. As a result, the domain width increases exponentially to eventually exceed the nanosheet size.[60] When domain width is greater than the lateral size of nanosheet, a single-domain phase is stabilized by the magnetic anisotropy. As shown in Figure 5m, when the thickness is lower than ~40 nm, the domain width rapidly increases. It indicated a transition from a maze-domain phase of thicker nanosheet to a single-domain phase of the ultrathin limit,

https://doi.org/10.1021/acsami.3c02446
ACS Appl. Mater. Interfaces 2023, 15, 26148−26158

where magnetic anisotropy dominates, although no single-domain nanosheets were observed.[58] This phenomenon is actually a reflection of the exchange interaction, the magnetic anisotropy, and the dipolar interaction per unit area in 2D Cr_5Te_8, which scale differently with the nanosheet thickness.[58,61]

Figure 5n show the corresponding thickness-dependent MFM signals. The domain contrast increases significantly with increasing the nanosheet thickness and finally becomes stable while the thickness exceeds 90 nm. When the thickness is 20 nm, the domain contrast is only 1.4°, and when the thickness is 90 nm, the domain contrast rapidly increases to 19.0°. While the nanosheet thickness exceeds 90 nm, due to the limited probe depth of the MFM tip, the contribution of the Cr atom at the bottom of the nanosheet to the magnetic signal becomes too weak. As a result, the domain contrast tends to be stable with increasing thickness which is larger than 90 nm. To our best knowledge, this is first time to report the strong thickness-dependent behavior of the domain width and domain contrast, which provides a good prospect for the application of 2D Cr_5Te_8 in magnetic memory devices and related fields and also provides a reference for the study of the magnetic domain structure of other chromium-based tellurides.

In addition to the magnetic domain structure of 2D Cr_5Te_8 at 2 K, we found another magnetic domain structure at 90 K, magnetic bubbles. We characterized the magnetic domain structure of a single 40 nm thickness nanosheet by MFM after ZFC, whose corresponding AFM morphology is present in Figure 5e. Figure 6a–l (Figure S8) shows the MFM images under different additional magnetic fields. We found that the magnetic domain structure of the Cr_5Te_8 nanosheet cooled to 90 K from room temperature after ZFC was completely different from that cooled to 2 K, as shown in Figures 5f and 6a. The magnetic domain structure at 2 K was a maze-like domain, while the domain structure at 90 K shows that several small magnetic bubbles with dark contrast appear within the large domain with bright contrast, and the diameter of each magnetic bubble is approximately 500 nm, which may be skyrmions. It was also discovered recently in other chromium-based tellurides such as $Cr_{1+\delta}Te_2$ ($\delta \approx 0.3$),[62] Cr_3Te_4,[63] and $Cr_{0.87}Te$.[64] Furthermore, we observed the evolution of the magnetic bubbles with an external magnetic field. With an upward additional magnetic field vertically to the *ab*-plane applied to the nanosheet, we found that when the value of the additional magnetic field was within the range of 0–70 mT, the magnetic bubbles existed stably. Based on their stability, we think that the magnetic bubbles are probably skyrmions.[62−64] As the additional magnetic field increased to 80 mT, the two magnetic bubbles in the center merge together. When the additional magnetic field is increased to 90 mT, the dark domain expands to cover most of the region of the Cr_5Te_8 nanosheet, and a new inverse magnetic bubble is formed in the dark domain. When the additional magnetic field is increased to 100 mT, the expanded dark domain completely covers the entire Cr_5Te_8 nanosheet, and the reverse magnetic bubble is stable in the additional magnetic field of 90–120 mT. Until the additional magnetic field continues to increase to 130 mT, the reverse magnetic bubble disappears, and the magnetic domain of the Cr_5Te_8 nanosheet reaches saturation, forming a single domain. Our results provide the first observation of the structure and evolution of magnetic bubbles in 2D Cr_5Te_8, which broadens the large family of magnetic bubbles materials and provides an important reference for studying other chromium-based tellurides.

3. CONCLUSIONS

In summary, we have successfully synthesized high-quality Cr_5Te_8 nanosheets and observed two magnetic domain structures: maze-like magnetic domains and magnetic bubbles. Simultaneously, the growth temperature and source−substrate distance are the key growth parameters to modulate the size of Cr_5Te_8 nanosheets. The Cr_5Te_8 nanosheets exhibit a lateral size of up to ≈300 μm and a thickness as low as ≈1.2 nm. Furthermore, the synthesized Cr_5Te_8 nanosheets possess both out-of-plane and in-plane ferromagnetism with T_C of 176 K, which is lower than those previously reported in bulk samples. Further MFM characterizations successfully observed thickness-dependent magnetic behavior of the maze-like magnetic domains and evolution of magnetic bubbles in Cr_5Te_8 nanosheets. The maze-like magnetic domains originate from alternating up and down magnetic domains, whose width increasing rapidly with decreasing sample thickness. This suggested a transition from a prevailing dominance of dipolar interactions to one governed by magnetic anisotropy. We believe this work paves the way for controllable growth of 2D magnetic materials by CVD and may provide a new platform for 2D-limited magnetic domain structures in magnetic memory devices.

4. EXPERIMENTAL METHODS

Growth of 2D Cr_5Te_8 Nanosheets. The growth of 2D Cr_5Te_8 nanosheets was performed in a two-zone tube furnace equipped with a 1 in. diameter quartz tube by atmospheric pressure chemical vapor deposition (APCVD). Tellurium powder (400 mg, Alfa Aesar, purity 99.99%) was placed upstream in the first zone which was heated to 550 °C. The mixed powders of $CrCl_3$ (8 mg, Alfa Aesar, purity 99.9%) and NaCl (1 mg, Alfa Aesar, purity 99.99%) were placed in the second zone, and the growth temperature was set within the range of 650–850 °C. Then a freshly cleaved mica substrate (fluorophlogopite ($KMg_3(AlSi_3O_{10})F_2$)), a fresh and clean SiO_2/Si substrate (280 nm thick SiO_2), or a sapphire substrate, used as growth substrate, was kept near the powder of $CrCl_3$. Prior to growth, the quartz tube was vacuumed and purged by Ar gas twice to remove the residue of oxygen and moisture. 95 sccm argon and 5 sccm hydrogen gas were used to transport the vapor species to the downstream substrates, and the growth time was 10 min under ambient pressure.

Transfer of 2D Cr_5Te_8 Nanosheets. The as-grown Cr_5Te_8 nanosheets on mica were transferred to the target substrates (SiO_2/Si or Au covered SiO_2/Si) using polystyrene (PS) as a medium for further characterization and MFM measurement. Briefly, Cr_5Te_8 nanosheets grown on mica substrates were first spin-coated with PS solution at a speed of 3000 rpm for 1 min and then baked on a hot plate at 60 °C for 30 min to improve the adhesion between the nanosheets and PS. The edges of the PS film were then scraped off with tweezers before being placed on the water surface. After the PS/Cr_5Te_8 was successfully transferred to the target substrate, it was baked at 80 °C for 20 min. Finally, the PS was removed with acetone.

Structure and Composition Characterization. The morphology and thickness of Cr_5Te_8 nanosheets were characterized by OM (6XB-PC, Shang Guang), SEM (NOVA NANOSEM450, FEI), and AFM (Dimension ICON, Bruker). The phase structure of the obtained nanosheets was analyzed by XRD (D8 ADVANCE, Bruker). The elemental composition and distribution were evaluated by EDS (X-MaxN 50 mm^2, Oxford Instruments) in the SEM. The vibration modes were ascertained with a confocal Raman microscope (alpha300 R, WITec). The elemental composition of Cr_5Te_8 nanosheets was analyzed by XPS (ESCALAB 250Xi, ThermoFisher Scientific).

https://doi.org/10.1021/acsami.3c02446
ACS Appl. Mater. Interfaces 2023, 15, 26148−26158

Magnetic Property Measurements. The measurements of magnetic susceptibility and T_C were performed in a magnetic property measurement system (MPMS3, Quantum Design), in which the anisotropic magnetic properties of samples grown on mica substrates were observed separately. The temperature-dependent magnetic susceptibility for out-of-plane and in-plane magnetic fields was measured within the temperature range from 1.8 to 300 K by the processes of ZFC and FC with a field of 1000 Oe, respectively. The field-dependent magnetization studies were performed with applied field range from −20000 to +20000 Oe at temperatures of 2, 100, and 200 K for out-of-plane and in-plane in several. Besides, the measurement was performed in DC mode, in which the samples were scanned vertically 30 mm in 4 s, and the gradients of magnetic field and temperature were set as 100 Oe s^{-1} and 2 K min^{-1} with the same intervals of 100 Oe and 0.2 K, respectively.

Magnetic Force Microscopy (MFM) Measurements. The MFM experiments were captured by a commercial MFM (attoAFM I, attocube) using a commercial magnetic tip (Nanosensors, PPP-MFMR, quality factor around 1800 at 2 K) based on a closed-cycle He cryostat (attoDRY2100, attocube). The scanning probe system was operated at the resonance frequency of the magnetic tip, approximately 75 kHz. The MFM images were taken in constant height mode with the scanning plane nominally ∼150 (200) nm above the substrate surface. The MFM signal, i.e., the change in the cantilever phase, is proportional to the out-of-plane stray field gradient. The dark (bright) regions in the MFM images represent attractive (repulsive) magnetization, where the magnetization is parallel (antiparallel) to the magnetic tip moments.

■ ASSOCIATED CONTENT

Data Availability Statement

The data sets generated and/or analyzed during this study are available from the corresponding author upon reasonable request.

Supporting Information

The Supporting Information is available free of charge at https://pubs.acs.org/doi/10.1021/acsami.3c02446.

> Schematic diagram of CVD growth process for 2D Cr_5Te_8 nanosheets on SiO_2/Si substrates, typical OM images of 2D Cr_5Te_8 nanosheets grown on different substrates, OM and SEM images of 2D Cr_5Te_8 nanosheets corresponding to AFM morphologies, OM image and AFM morphology of a typical hexagonal stacking Cr_5Te_8 nanosheet, $M-T$ and $M-H$ measurements of thinner samples, maze-like magnetic domains and evolution, maze-like magnetic domains of Cr_5Te_8 nanosheets with different thicknesses, magnetic bubbles and evolution (PDF)

■ AUTHOR INFORMATION

Corresponding Authors

Fei Pang − *Beijing Key Laboratory of Optoelectronic Functional Materials & Micro-nano Devices, Department of Physics, Renmin University of China, Beijing 100872, China;* orcid.org/0000-0002-8578-366X; Email: feipang@ruc.edu.cn

Zhihai Cheng − *Beijing Key Laboratory of Optoelectronic Functional Materials & Micro-nano Devices, Department of Physics, Renmin University of China, Beijing 100872, China;* orcid.org/0000-0003-4938-4490; Email: zhihaicheng@ruc.edu.cn

Authors

Hanxiang Wu − *Beijing Key Laboratory of Optoelectronic Functional Materials & Micro-nano Devices, Department of Physics, Renmin University of China, Beijing 100872, China*

Jianfeng Guo − *Beijing Key Laboratory of Optoelectronic Functional Materials & Micro-nano Devices, Department of Physics, Renmin University of China, Beijing 100872, China*

Suonan Zhaxi − *Beijing Key Laboratory of Optoelectronic Functional Materials & Micro-nano Devices, Department of Physics, Renmin University of China, Beijing 100872, China*

Hua Xu − *Beijing Key Laboratory of Optoelectronic Functional Materials & Micro-nano Devices, Department of Physics, Renmin University of China, Beijing 100872, China*

Shuo Mi − *Beijing Key Laboratory of Optoelectronic Functional Materials & Micro-nano Devices, Department of Physics, Renmin University of China, Beijing 100872, China*

Le Wang − *Beijing Key Laboratory of Optoelectronic Functional Materials & Micro-nano Devices, Department of Physics, Renmin University of China, Beijing 100872, China*

Shanshan Chen − *Beijing Key Laboratory of Optoelectronic Functional Materials & Micro-nano Devices, Department of Physics, Renmin University of China, Beijing 100872, China;* orcid.org/0000-0002-3155-8571

Rui Xu − *Beijing Key Laboratory of Optoelectronic Functional Materials & Micro-nano Devices, Department of Physics, Renmin University of China, Beijing 100872, China*

Wei Ji − *Beijing Key Laboratory of Optoelectronic Functional Materials & Micro-nano Devices, Department of Physics, Renmin University of China, Beijing 100872, China;* orcid.org/0000-0001-5249-6624

Complete contact information is available at: https://pubs.acs.org/10.1021/acsami.3c02446

Author Contributions

H.X.W. and J.F.G. contributed equally to this work. F.P. and Z.H.C. conceived and supervised the project. H.X.W. synthesized 2D Cr_5Te_8 nanosheets and performed characterization and MPMS measurements. J.F.G. performed MFM measurements. H.X. performed Raman characterization. All authors contributed to the data analysis. H.X.W., J.F.G. and F.P. wrote the manuscript with contributions from all authors.

Notes

The authors declare no competing financial interest.

■ ACKNOWLEDGMENTS

This project was supported by the National Natural Science Foundation of China (NSFC) (No. 61674045), the Ministry of Science and Technology (MOST) of China (No. 2016YFA0200700), the Strategic Priority Research Program and Key Research Program of Frontier Sciences (Chinese Academy of Sciences, CAS) (No. XDB30000000, No. QYZDB-SSW-SYS031), and the Fundamental Research Funds for the Central Universities and the Research Funds of Renmin University of China (No. 21XNLG27 and 22XNH097).

■ REFERENCES

(1) Zhong, D.; Seyler, K. L.; Linpeng, X.; Cheng, R.; Sivadas, N.; Huang, B.; Schmidgall, E.; Taniguchi, T.; Watanabe, K.; McGuire, M. A.; Yao, W.; Xiao, D.; Fu, K. C.; Xu, X. Van der Waals Engineering of Ferromagnetic Semiconductor Heterostructures for Spin and Valleytronics. *Sci. Adv.* **2017**, *3*, No. e1603113.

(2) Lin, X.; Yang, W.; Wang, K. L.; Zhao, W. Two-Dimensional Spintronics for Low-Power Electronics. *Nat. Electron.* **2019**, *2*, 274−283.
(3) Akinwande, D.; Petrone, N.; Hone, J. Two-Dimensional Flexible Nanoelectronics. *Nat. Commun.* **2014**, *5*, 5678.
(4) Lin, Z.; Liu, Y.; Halim, U.; Ding, M.; Liu, Y.; Wang, Y.; Jia, C.; Chen, P.; Duan, X.; Wang, C.; Song, F.; Li, M.; Wan, C.; Huang, Y.; Duan, X. Solution-Processable 2D Semiconductors for High-Performance Large-Area Electronics. *Nature* **2018**, *562*, 254−258.
(5) Wang, Q. H.; Kalantar-Zadeh, K.; Kis, A.; Coleman, J. N.; Strano, M. S. Electronics and Optoelectronics of Two-Dimensional Transition Metal Dichalcogenides. *Nat. Nanotechnol.* **2012**, *7*, 699−712.
(6) Kim, E.; Lee, Y.; Ko, C.; Park, Y.; Yeo, J.; Chen, Y.; Choe, H. S.; Allen, F. I.; Rho, J.; Tongay, S.; Wu, J.; Kim, K.; Grigoropoulos, C. P. Tuning the Optical and Electrical Properties of MoS_2 by Selective Ag Photo-Reduction. *Appl. Phys. Lett.* **2018**, *113*, 013105.
(7) Hossain, M.; Qin, B.; Li, B.; Duan, X. Synthesis, Characterization, Properties and Applications of Two-Dimensional Magnetic Materials. *Nano Today* **2022**, *42*, 101338.
(8) Klein, D. R.; MacNeill, D.; Lado, J. L.; Soriano, D.; Navarro-Moratalla, E.; Watanabe, K.; Taniguchi, T.; Manni, S.; Canfield, P.; Fernandez-Rossier, J.; Jarillo-Herrero, P. Probing Magnetism in 2D van der Waals Crystalline Insulators via Electron Tunneling. *Science* **2018**, *360*, 1218−1222.
(9) Huang, B.; Clark, G.; Navarro-Moratalla, E.; Klein, D. R.; Cheng, R.; Seyler, K. L.; Zhong, D.; Schmidgall, E.; McGuire, M. A.; Cobden, D. H.; Yao, W.; Xiao, D.; Jarillo-Herrero, P.; Xu, X. Layer-Dependent Ferromagnetism in a van der Waals Crystal Down to the Monolayer Limit. *Nature* **2017**, *546*, 270−273.
(10) Fei, Z.; Huang, B.; Malinowski, P.; Wang, W.; Song, T.; Sanchez, J.; Yao, W.; Xiao, D.; Zhu, X.; May, A. F.; Wu, W.; Cobden, D. H.; Chu, J. H.; Xu, X. Two-Dimensional Itinerant Ferromagnetism in Atomically Thin Fe_3GeTe_2. *Nat. Mater.* **2018**, *17*, 778−782.
(11) Deng, Y.; Yu, Y.; Song, Y.; Zhang, J.; Wang, N. Z.; Sun, Z.; Yi, Y.; Wu, Y. Z.; Wu, S.; Zhu, J.; Wang, J.; Chen, X. H.; Zhang, Y. Gate-Tunable Room-Temperature Ferromagnetism in Two-Dimensional Fe_3GeTe_2. *Nature* **2018**, *563*, 94−99.
(12) Yin, S.; Zhao, L.; Song, C.; Huang, Y.; Gu, Y.; Chen, R.; Zhu, W.; Sun, Y.; Jiang, W.; Zhang, X.; Pan, F. Evolution of Domain Structure in Fe_3GeTe_2. *Chin. Phys. B* **2021**, *30*, 027505.
(13) Zhang, G.; Wu, H.; Zhang, L.; Zhang, S.; Yang, L.; Gao, P.; Wen, X.; Jin, W.; Guo, F.; Xie, Y.; Li, H.; Tao, B.; Zhang, W.; Chang, H. Highly-Tunable Intrinsic Room-Temperature Ferromagnetism in 2D van der Waals Semiconductor $Cr_xGa_{1-x}Te$. *Adv. Sci.* **2022**, *9*, 2103173.
(14) Luo, S.; Zhu, X.; Liu, H.; Song, S.; Chen, Y.; Liu, C.; Zhou, W.; Tang, C.; Shao, G.; Jin, Y.; Guan, J.; Tung, V. C.; Li, H.; Chen, X.; Ouyang, F.; Liu, S. Direct Growth of Magnetic Non-van der Waals Cr_2X_3(X = S, Se, and Te) on SiO_2/Si Substrates through the Promotion of KOH. *Chem. Mater.* **2022**, *34*, 2342−2351.
(15) Habib, M. R.; Wang, S.; Wang, W.; Xiao, H.; Obaidulla, S. M.; Gayen, A.; Khan, Y.; Chen, H.; Xu, M. Electronic Properties of Polymorphic Two-Dimensional Layered Chromium Disulphide. *Nanoscale* **2019**, *11*, 20123−20132.
(16) Zhu, X.; Liu, H.; Liu, L.; Ren, L.; Li, W.; Fang, L.; Chen, X.; Xie, L.; Jing, Y.; Chen, J.; Liu, S.; Ouyang, F.; Zhou, Y.; Xiong, X. Spin Glass State in Chemical Vapor-Deposited Crystalline Cr_2Se_3 Nanosheets. *Chem. Mater.* **2021**, *33*, 3851−3858.
(17) Zhang, D.; Yi, C.; Ge, C.; Shu, W.; Li, B.; Duan, X.; Pan, A.; Wang, X. Controlled Vapor Growth of 2D Magnetic Cr_2Se_3 and Its Magnetic Proximity Effect in Heterostructures. *Chin. Phys. B* **2021**, *30*, 097601.
(18) Zhang, Y.; Chu, J.; Yin, L.; Shifa, T. A.; Cheng, Z.; Cheng, R.; Wang, F.; Wen, Y.; Zhan, X.; Wang, Z.; He, J. Ultrathin Magnetic 2D Single-Crystal CrSe. *Adv. Mater.* **2019**, *31*, 1900056.
(19) Meng, L.; Zhou, Z.; Xu, M.; Yang, S.; Si, K.; Liu, L.; Wang, X.; Jiang, H.; Li, B.; Qin, P.; Zhang, P.; Wang, J.; Liu, Z.; Tang, P.; Ye, Y.; Zhou, W.; Bao, L.; Gao, H.-J.; Gong, Y. Anomalous Thickness Dependence of Curie Temperature in Air-Stable Two-Dimensional Ferromagnetic 1T-$CrTe_2$ Grown by Chemical Vapor Deposition. *Nat. Commun.* **2021**, *12*, 809.
(20) Sun, X.; Li, W.; Wang, X.; Sui, Q.; Zhang, T.; Wang, Z.; Liu, L.; Li, D.; Feng, S.; Zhong, S.; Wang, H.; Bouchiat, V.; Nunez Regueiro, M.; Rougemaille, N.; Coraux, J.; Purbawati, A.; Hadj-Azzem, A.; Wang, Z.; Dong, B.; Wu, X.; et al. Room Temperature Ferromagnetism in Ultra-Thin van der Waals Crystals of 1T-$CrTe_2$. *Nano Res.* **2020**, *13*, 3358−3363.
(21) Wu, H.; Zhang, W.; Yang, L.; Wang, J.; Li, J.; Li, L.; Gao, Y.; Zhang, L.; Du, J.; Shu, H.; Chang, H. Strong Intrinsic Room-Temperature Ferromagnetism in Freestanding Non-van der Waals Ultrathin 2D Crystals. *Nat. Commun.* **2021**, *12*, 5688.
(22) Wang, M.; Kang, L.; Su, J.; Zhang, L.; Dai, H.; Cheng, H.; Han, X.; Zhai, T.; Liu, Z.; Han, J. Two-Dimensional Ferromagnetism in CrTe Flakes Down to Atomically Thin Layers. *Nanoscale* **2020**, *12*, 16427−16432.
(23) Coughlin, A. L.; Xie, D.; Yao, Y.; Zhan, X.; Chen, Q.; Hewa-Walpitage, H.; Zhang, X.; Guo, H.; Zhou, H.; Lou, J.; Wang, J.; Li, Y. S.; Fertig, H. A.; Zhang, S. Near Degeneracy of Magnetic Phases in Two-Dimensional Chromium Telluride with Enhanced Perpendicular Magnetic Anisotropy. *ACS Nano* **2020**, *14*, 15256−15266.
(24) Roy, A.; Guchhait, S.; Dey, R.; Pramanik, T.; Hsieh, C. C.; Rai, A.; Banerjee, S. K. Perpendicular Magnetic Anisotropy and Spin Glass-Like Behavior in Molecular Beam Epitaxy Grown Chromium Telluride Thin Films. *ACS Nano* **2015**, *9*, 3772−3779.
(25) Li, H.; Wang, L.; Chen, J.; Yu, T.; Zhou, L.; Qiu, Y.; He, H.; Ye, F.; Sou, I. K.; Wang, G. Molecular Beam Epitaxy Grown Cr_2Te_3 Thin Films with Tunable Curie Temperatures for Spintronic Devices. *ACS Appl. Nano Mater.* **2019**, *2*, 6809−6817.
(26) Bian, M.; Kamenskii, A. N.; Han, M.; Li, W.; Wei, S.; Tian, X.; Eason, D. B.; Sun, F.; He, K.; Hui, H.; Yao, F.; Sabirianov, R.; Bird, J. P.; Yang, C.; Miao, J.; Lin, J.; Crooker, S. A.; Hou, Y.; Zeng, H. Covalent 2D Cr_2Te_3 Ferromagnet. *Mater. Res. Lett.* **2021**, *9*, 205−212.
(27) Zhong, J.; Wang, M.; Liu, T.; Zhao, Y.; Xu, X.; Zhou, S.; Han, J.; Gan, L.; Zhai, T. Strain-Sensitive Ferromagnetic Two-Dimensional Cr_2Te_3. *Nano Res.* **2022**, *15*, 1254−1259.
(28) Wen, Y.; Liu, Z.; Zhang, Y.; Xia, C.; Zhai, B.; Zhang, X.; Zhai, G.; Shen, C.; He, P.; Cheng, R.; Yin, L.; Yao, Y.; Getaye Sendeku, M.; Wang, Z.; Ye, X.; Liu, C.; Jiang, C.; Shan, C.; Long, Y.; He, J. Tunable Room-Temperature Ferromagnetism in Two-Dimensional Cr_2Te_3. *Nano Lett.* **2020**, *20*, 3130−3139.
(29) Guo, Y.; Kang, L.; Yu, S.; Yang, J.; Qi, X.; Zhang, Z.; Liu, Z. CVD Growth of Large-Scale and Highly Crystalline 2D Chromium Telluride Nanoflakes. *ChemNanoMat* **2021**, *7*, 323−327.
(30) Coughlin, A. L.; Xie, D.; Zhan, X.; Yao, Y.; Deng, L.; Hewa-Walpitage, H.; Bontke, T.; Chu, C. W.; Li, Y.; Wang, J.; Fertig, H. A.; Zhang, S. Van der Waals Superstructure and Twisting in Self-Intercalated Magnet with Near Room-Temperature Perpendicular Ferromagnetism. *Nano Lett.* **2021**, *21*, 9517−9525.
(31) Wang, W.; Fan, J.; Liu, H.; Zheng, H.; Ma, C.; Zhang, L.; Sun, Y.; Wang, C.; Zhu, Y.; Yang, H. Fabrication and Magnetic-Electronic Properties of van der Waals Cr_4Te_5 Ferromagnetic Films. *CrystEngComm* **2022**, *24*, 674−680.
(32) Chen, C.; Chen, X.; Wu, C.; Wang, X.; Ping, Y.; Wei, X.; Zhou, X.; Lu, J.; Zhu, L.; Zhou, J.; Zhai, T.; Han, J.; Xu, H. Air-Stable 2D Cr_5Te_8 Nanosheets with Thickness-Tunable Ferromagnetism. *Adv. Mater.* **2022**, *34*, 2107512.
(33) Jin, Z.; Ji, Z.; Zhong, Y.; Jin, Y.; Hu, X.; Zhang, X.; Zhu, L.; Huang, X.; Li, T.; Cai, X.; Zhou, L. Controlled Synthesis of a Two-Dimensional Non-van der Waals Ferromagnet toward a Magnetic Moiré Superlattice. *ACS Nano* **2022**, *16*, 7572−7579.
(34) Bian, M.; Zhu, L.; Wang, X.; Choi, J.; Chopdekar, R. V.; Wei, S.; Wu, L.; Huai, C.; Marga, A.; Yang, Q.; Li, Y. C.; Yao, F.; Yu, T.; Crooker, S. A.; Cheng, X. M.; Sabirianov, R. F.; Zhang, S.; Lin, J.; Hou, Y.; Zeng, H. Dative Epitaxy of Commensurate Monocrystalline Covalent van der Waals Moiré Supercrystal. *Adv. Mater.* **2022**, *34*, 2200117.

https://doi.org/10.1021/acsami.3c02446
ACS Appl. Mater. Interfaces 2023, 15, 26148−26158

(35) Tang, B.; Wang, X.; Han, M.; Xu, X.; Zhang, Z.; Zhu, C.; Cao, X.; Yang, Y.; Fu, Q.; Yang, J.; Li, X.; Gao, W.; Zhou, J.; Lin, J.; Liu, Z. Phase Engineering of Cr_5Te_8 with Colossal Anomalous Hall Effect. *Nat. Electron.* **2022**, *5*, 224−232.
(36) Niu, K.; Qiu, G.; Wang, C.; Li, D.; Niu, Y.; Li, S.; Kang, L.; Cai, Y.; Han, M.; Lin, J. Self-Intercalated Magnetic Heterostructures in 2D Chromium Telluride. *Adv. Funct. Mater.* **2023**, *33*, 2208528.
(37) Huang, Z.-L.; Kockelmann, W.; Telling, M.; Bensch, W. A Neutron Diffraction Study of Structural and Magnetic Properties of Monoclinic Cr_5Te_8. *Solid State Sci.* **2008**, *10*, 1099−1105.
(38) Lukoschus, K.; Kraschinski, S.; Näther, C.; Bensch, W.; Kremer, R. K. Magnetic Properties and Low Temperature X-Ray Studies of the Weak Ferromagnetic Monoclinic and Trigonal Chromium Tellurides Cr_5Te_8. *J. Solid State Chem.* **2004**, *177*, 951−959.
(39) Zhang, X.; Yu, T.; Xue, Q.; Lei, M.; Jiao, R. Critical Behavior and Magnetocaloric Effect in Monoclinic Cr_5Te_8. *J. Alloys Compd.* **2018**, *750*, 798−803.
(40) Xie, L.; Wang, J.; Li, J.; Li, C.; Zhang, Y.; Zhu, B.; Guo, Y.; Wang, Z.; Zhang, K. An Atomically Thin Air-Stable Narrow-Gap Semiconductor Cr_2S_3 for Broadband Photodetection with High Responsivity. *Adv. Electron. Mater.* **2021**, *7*, 2000962.
(41) Cui, F.; Zhao, X.; Tang, B.; Zhu, L.; Huan, Y.; Chen, Q.; Liu, Z.; Zhang, Y. Epitaxial Growth of Step-Like Cr_2S_3 Lateral Homojunctions Towards Versatile Conduction Polarities and Enhanced Transistor Performances. *Small* **2022**, *18*, 2105744.
(42) Zhou, S.; Wang, R.; Han, J.; Wang, D.; Li, H.; Gan, L.; Zhai, T. Ultrathin Non-van der Waals Magnetic Rhombohedral Cr_2S_3: Space-Confined Chemical Vapor Deposition Synthesis and Raman Scattering Investigation. *Adv. Funct. Mater.* **2019**, *29*, 1805880.
(43) Cui, F.; Zhao, X.; Xu, J.; Tang, B.; Shang, Q.; Shi, J.; Huan, Y.; Liao, J.; Chen, Q.; Hou, Y.; Zhang, Q.; Pennycook, S. J.; Zhang, Y. Controlled Growth and Thickness-Dependent Conduction-Type Transition of 2D Ferrimagnetic Cr_2S_3 Semiconductors. *Adv. Mater.* **2020**, *32*, 1905896.
(44) Chu, J.; Zhang, Y.; Wen, Y.; Qiao, R.; Wu, C.; He, P.; Yin, L.; Cheng, R.; Wang, F.; Wang, Z.; Xiong, J.; Li, Y.; He, J. Sub-Millimeter-Scale Growth of One-Unit-Cell-Thick Ferrimagnetic Cr_2S_3 Nanosheets. *Nano Lett.* **2019**, *19*, 2154−2161.
(45) Li, N.; Zhu, L.; Shang, H.; Wang, F.; Zhang, Y.; Yao, Y.; Wang, J.; Zhan, X.; Wang, F.; He, J.; Wang, Z. Controlled Synthesis and Raman Study of a 2D Antiferromagnetic P-Type Semiconductor: Alpha-MnSe. *Nanoscale* **2021**, *13*, 6953−6964.
(46) Zou, J.; Yang, Y.; Hu, D.; Kang, L.; Zhu, C.; Tian, D.; Lv, X.; Kutty, G.; Guo, Y.; Xu, M.; Li, F.; Hong, G.; Liu, Z. Controlled Growth of Ultrathin Ferromagnetic β-MnSe Semiconductor. *SmartMat* **2022**, *3*, 482−490.
(47) Zhao, Z.; Zhou, J.; Liu, L.; Liu, N.; Huang, J.; Zhang, B.; Li, W.; Zeng, Y.; Zhang, T.; Ji, W.; Yang, T.; Zhang, Z.; Li, S.; Hou, Y. Two-Dimensional Room-Temperature Magnetic Nonstoichiometric Fe_7Se_8 Nanocrystals: Controllable Synthesis and Magnetic Behavior. *Nano Lett.* **2022**, *22*, 1242−1250.
(48) Ma, H.; Wan, Z.; Li, J.; Wu, R.; Zhang, Z.; Li, B.; Zhao, B.; Qian, Q.; Liu, Y.; Xia, Q.; Guo, G.; Duan, X.; Duan, X. Phase-Tunable Synthesis of Ultrathin Layered Tetragonal CoSe and Nonlayered Hexagonal CoSe Nanoplates. *Adv. Mater.* **2019**, *31*, 1900901.
(49) Liu, Y.; Abeykoon, M.; Stavitski, E.; Attenkofer, K.; Petrovic, C. Magnetic Anisotropy and Entropy Change in Trigonal Cr_5Te_8. *Phys. Rev. B* **2019**, *100*, 245114.
(50) Burton, W.; Cabrera, N. Crystal Growth and Surface Structure. Part I. *Discuss. Faraday Soc.* **1949**, *5*, 33−39.
(51) Haraldsen, H.; Neuber, A. A. Magnetochemische Untersuchungen. XXVII. Magnetische und röntgenographische Untersuchungen am System Chrom-Tellur. *Z. Anorg. Allg. Chem.* **1937**, *234*, 353−371.
(52) Andresen, A. F.; et al. A Neutron Diffraction Investigation of Cr_2Te_3 and Cr_5Te_6. *Acta Chem. Scand.* **1963**, *17*, 1335−1342.
(53) Guo, J.; Wang, H.; Wang, X.; Gu, S.; Mi, S.; Zhu, S.; Hu, J.; Pang, F.; Ji, W.; Gao, H.-J.; Xia, T.; Cheng, Z. Coexisting Ferromagnetic-Antiferromagnetic Phases and Manipulation in a Magnetic Topological Insulator $MnBi_4Te_7$. *J. Phys. Chem. C* **2022**, *126*, 13884−13893.
(54) Serri, M.; Cucinotta, G.; Poggini, L.; Serrano, G.; Sainctavit, P.; Strychalska-Nowak, J.; Politano, A.; Bonaccorso, F.; Caneschi, A.; Cava, R. J.; Sessoli, R.; Ottaviano, L.; Klimczuk, T.; Pellegrini, V.; Mannini, M. Enhancement of the Magnetic Coupling in Exfoliated $CrCl_3$ Crystals Observed by Low-Temperature Magnetic Force Microscopy and X-Ray Magnetic Circular Dichroism. *Adv. Mater.* **2020**, *32*, 2000566.
(55) Van Schendel, P. J. A.; Hug, H. J.; Stiefel, B.; Martin, S.; Guntherodt, H. J. A Method for the Calibration of Magnetic Force Microscopy Tips. *J. Appl. Phys.* **2000**, *88*, 435−445.
(56) Kittel, C. Physical Theory of Ferromagnetic Domains. *Rev. Mod. Phys.* **1949**, *21*, 541.
(57) Kashuba, A. B.; Pokrovsky, V. L. Stripe Domain Structures in a Thin Ferromagnetic Film. *Phys. Rev. B* **1993**, *48*, 10335−10344.
(58) Li, Q.; Yang, M.; Gong, C.; Chopdekar, R. V.; N'Diaye, A. T.; Turner, J.; Chen, G.; Scholl, A.; Shafer, P.; Arenholz, E.; Schmid, A. K.; Wang, S.; Liu, K.; Gao, N.; Admasu, A. S.; Cheong, S. W.; Hwang, C.; Li, J.; Wang, F.; Zhang, X.; et al. Patterning-Induced Ferromagnetism of Fe_3GeTe_2 van der Waals Materials beyond Room Temperature. *Nano Lett.* **2018**, *18*, 5974−5980.
(59) Yafet, Y.; Gyorgy, E. M. Ferromagnetic Strip Domains in an Atomic Monolayer. *Phys. Rev. B* **1988**, *38*, 9145−9151.
(60) Wu, Y. Z.; Won, C.; Scholl, A.; Doran, A.; Zhao, H. W.; Jin, X. F.; Qiu, Z. Q. Magnetic Stripe Domains in Coupled Magnetic Sandwiches. *Phys. Rev. Lett.* **2004**, *93*, 117205.
(61) Won, C.; Wu, Y. Z.; Choi, J.; Kim, W.; Scholl, A.; Doran, A.; Owens, T.; Wu, J.; Jin, X. F.; Zhao, H. W.; Qiu, Z. Q. Magnetic Stripe Melting at the Spin Reorientation Transition in Fe/Ni/Cu(001). *Phys. Rev. B* **2005**, *71*, 224429.
(62) Saha, R.; Meyerheim, H. L.; Gobel, B.; Hazra, B. K.; Deniz, H.; Mohseni, K.; Antonov, V.; Ernst, A.; Knyazev, D.; Bedoya-Pinto, A.; Mertig, I.; Parkin, S. S. P. Observation of Néel-Type Skyrmions in Acentric Self-Intercalated $Cr_{1+\delta}Te_2$. *Nat. Commun.* **2022**, *13*, 3965.
(63) Li, B.; Deng, X.; Shu, W.; Cheng, X.; Qian, Q.; Wan, Z.; Zhao, B.; Shen, X.; Wu, R.; Shi, S.; Zhang, H.; Zhang, Z.; Yang, X.; Zhang, J.; Zhong, M.; Xia, Q.; Li, J.; Liu, Y.; Liao, L.; Ye, Y.; et al. Air-Stable Ultrathin Cr_3Te_4 Nanosheets with Thickness-Dependent Magnetic Biskyrmions. *Mater. Today* **2022**, *57*, 66−74.
(64) Liu, J.; Ding, B.; Liang, J.; Li, X.; Yao, Y.; Wang, W. Magnetic Skyrmionic Bubbles at Room Temperature and Sign Reversal of the Topological Hall Effect in a Layered Ferromagnet $Cr_{0.87}Te$. *ACS Nano* **2022**, *16*, 13911−13918.

https://doi.org/10.1021/acsami.3c02446
ACS Appl. Mater. Interfaces 2023, 15, 26148−26158